19e Journées de l'Hydrodynamique
26 – 28 novembre 2024, Nantes

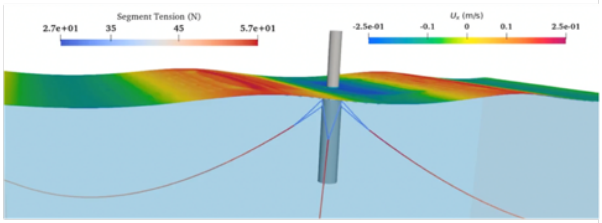


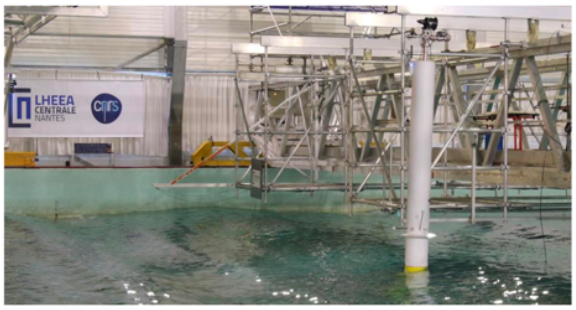


# ETUDE DES EFFETS DE LA HOULE SUR UNE HYDROLIENNE AVEC LE CODE VORTEX PARTICULAIRE DOROTHY

# *WAVE MODELLING IN VORTEX PARTICLE SOLVER DOROTHY: A TIDAL TURBINE STUDY*

**M.-A. DUFOUR[1,2], G. GERMAIN[2,*], G. PINON[1,*], E. RIVOALEN[1,3]**
[*] *Corresponding authors: gregory.germain@ifremer.fr, gregory.pinon@univ-lehavre.fr*

[1]Laboratoire Ondes et Milieux Complexes (LOMC) - Normandie Univ, UNIHAVRE, CNRS, 76600 Le Havre, France
[2]Laboratoire d'Hydrodynamique Marine (LHyMar), IFREMER, Centre Manche Mer du Nord, 62200 Boulogne-sur-Mer, France
[3]Laboratoire de Mécanique de Normandie (LMN) - Normandie Univ, INSA ROUEN, LMN, 76000 Rouen, France

**Résumé**

Ce papier présente l'intégration d'un modèle potentiel houle-courant de Stokes à l'ordre un au code Dorothy dont le coeur est la résolution lagrangienne des équations de Navier-Stokes dans leur formulation vitesse-vorticité. Pour représenter une hydrolienne, les pales sont figurées en ligne portante. La méthode présentée ici permet de montrer que les performances moyennes d'une hydrolienne restent inchangées lorsque celle-ci est soumise aux effets combinés de la houle et du courant. Cependant, les fluctuations de performances augmentent fortement avec la houle et sont corrélées avec la vitesse réduite de la turbine. Cette méthode permet également d'étudier les effets de la houle en propagation co- et contre-courant sur le développement du sillage. Des oscillations périodiques associées à la houle y sont mises en évidence.

**Summary**

In this paper, the validation of a Stokes first order wave-current model is performed after having detailed its implementation on top of the Lagrangian vortex particle (VP) Navier-Stokes solver named Dorothy. The results show that the lifting-line (LL) turbine blades provide accurate loads evaluation under wave conditions. Averaged performance remains unaffected by waves but with a significant increase of standard deviations correlated with an increasing tip speed ratio. This method also makes it possible to study the development of the wake in the presence of following and opposing current waves. Pulsations in the wake due to waves effect are evidenced.

# I – Introduction

Tidal energy reaches the pre-commercial development stage with the first arrays of turbines that will be deployed in the upcoming years. To cite a few examples, the 17 MW FloWatt and 12 MW NH1 farms located in the Alderney Race (Normandy) are expected to start up before the end of the decade. To speed up tidal farms deployment, an important task is to lower the risk of turbine failures at sea. To this end, one of the topics to be tackled is blade material fatigue and damage loads. Yet, a better understanding of the fluctuating loads from a fluid dynamic point of view is needed to enhance predictions in the material domain. Flow unsteadiness may be generated by the turbines interactions in an array and by the upstream turbulence. Another environmental condition triggering loads fluctuations is surface gravity waves inasmuch as they induce orbital velocities in the water column to a depth of half their wavelength.

Gravity waves effects upon horizontal axis tidal turbines performance have been studied both experimentally and numerically. Experimental studies state that gravity waves do not introduce a significant change in tidal turbine average performance [14, 10]. However, it is shown that waves generate major loads and performance fluctuations that contribute to blade material fatigue [6]. Those observations are further confirmed by several numerical studies in which the turbine is modelled using the blade element momentum theory (BEMT) [1] possibly modified to account for added mass loads [8] and dynamic stall [12, 20]. In those models, wave-induced velocities are generated using the Stokes first order wave-current model [1, 12]. To the authors' knowledge, gravity wave effect on horizontal axis tidal turbine wake is a more recent topic in both experimental [13] and numerical areas [17].

To contribute to the study of gravity waves impact on tidal turbines performance and wake dynamic, the authors present in this paper the implementation of a Stokes first order wave-current model into the in-house vortex particle Navier-Stokes solver Dorothy [16]. The present study focuses on describing the employed methodology, the validation of the wave-current model, and the analysis of performance and wake modifications generated by waves. Hence the presented methodology will be a reliable basis for further wake studies possibly with upstream turbulence and turbines array interaction.

# II – Methodology

## II – 1 Dorothy vortex particle (VP) solver with lifting-line (LL)

In the vortex particle method, the fluid domain is discretised into $N \in \mathbb{N}$ particles which depend upon the local velocity ($\vec{u}$) and vorticity ($\vec{\nabla} \wedge \vec{u} = \vec{\omega}$) fields. It is a fully Lagrangian method with the time ($t$) as only variable. The $i$-th fluid particle properties: position ($\vec{X}_i(t)$), velocity ($\vec{U}_i(t) = \vec{u}(\vec{X}_i(t), t)$), time-independent volume ($V_i$) and vorticity weight ($\vec{\Omega}_i(t) = \iiint_{V_i} \vec{\omega} \mathrm{d}v$). Uppercase letters are specifically reserved for fluid particles related quantities. Time evolution of those properties is described by the discretised Lagrangian velocity-vorticity Navier-Stokes equations [23]:

$$\frac{\mathrm{d}\vec{X}_i}{\mathrm{d}t}(t) = \vec{U}_i(t) = \vec{U}_i^{\phi}(t) + \vec{U}_i^{\psi}(t), \tag{1}$$

$$\frac{\mathrm{d}\vec{\Omega}_i}{\mathrm{d}t}(t) = \vec{S}_i(t)V_i + \vec{L}_i(t)V_i. \tag{2}$$

Helmholtz decomposition is applied to the velocity field (Eq. (1)). The rotational velocity component ($\vec{U}_i^{\psi}$) is the core of vortex particle methods. It is and derived from a divergence-free solenoidal vector potential field ($\vec{\psi}$) which is solution of a Poisson equation. It is evaluated by means of the Biot-Savart law (Eq. (3)) using a Winckelmans-Leonard regularized kernel ($\vec{K}_\varepsilon$) of smoothing parameter $\varepsilon$ [16, 23] and a *treecode* algorithm [16] to speed up the computation.

$$\vec{U}_i^{\psi}(t) \simeq \sum_{j=1}^{N} \vec{K}_\varepsilon \left( \vec{X}_i(t) - \vec{X}_j(t) \right) \wedge \vec{\Omega}_j(t) \tag{3}$$

The potential velocity component ($\vec{U}_i^{\phi}$, Eq. (4)) is derived from a scalar potential field ($\phi$) solution to a Laplace equation. It includes the mean upstream flow velocity ($\vec{u}^{\infty}$) and the Stokes first order wave-current orbital velocity ($\vec{u}^{w}$) detailed in subsection II – 2.

$$\vec{U}_i^{\phi} = \left[ \vec{u}^{\phi}\left(\vec{x},t\right) \right]_{\vec{x}=\vec{X}_i(t)} = u^{\infty}\vec{e}_x + \left[ \vec{u}^{w}\left(\vec{x},t\right) \right]_{\vec{x}=\vec{X}_i(t)} . \tag{4}$$

Two terms contribute to the momentum equation (Eq. (2)). First, the stretching term ($\vec{S}_i(t)V_i$) is evaluated with the transposed formulation to ensure the total vorticity conservation [2]. Second, the diffusion term ($\vec{L}_i(t)$) is computed via the particle strength exchange (PSE) method [5]. The diffusion term includes both molecular and turbulent diffusions to account for large eddy simulation (LES) modelling [16]. Eventually, Navier-Stokes equations (Eq. (1) and Eq. (2)) are integrated with a 2-nd or 4-th order Runge-Kutta algorithm. A redistribution of the particles is performed every few time-steps to prevent from a too wide distortion of the particles distribution to happen. This redistribution algorithm basically generates a new set of particles located on a 3D cartesian grid with the interpolated vorticity of the old particles.

Following an idea that recently emerged in the literature [21, 19, 22], a lifting-line blade representation has been added into the Dorothy VP solver to represent the turbine [7]. In this approach, the blade of length ($L_b$) is one-dimensional. It is discretised in $N_s \in \mathbb{N}$ sections of width ($\mathrm{d}r = L_b/N_s$). Each blade rotates at the angular velocity ($\omega_{rot}$). The distance between the blade root and the centre of rotation (denoted $(x_{rot}, y_{rot}, z_{rot})$) is called the hub radius ($R_h$). For each section, the vorticity generation is linked to the local lift coefficient by means of the Kutta-Joukovski theorem. Loads are then evaluated using tabulated lift and drag coefficients depending on the local angle of attack ($\alpha$). To circumvent overestimated loads at blades tip due to particles formalism, a tip correction is applied [7]. Then, local lift and drag are projected in the rotational direction ($\theta$) and normal-to-rotation direction ($x$) which provides the local loads $\mathrm{d}F_\theta$ and $\mathrm{d}F_x$. Integrating those loads distributions provides the turbine torque ($Q$) and thrust ($T$). Turbine performance, power ($C_P$) and thrust ($C_T$) coefficients are then assessed as follow:

$$C_P = \frac{\omega_{rot} Q}{\frac{1}{2}\rho\pi \left(L_b + R_h\right)^2 \left\|\vec{u}^{\infty}\right\|^3}, \qquad C_T = \frac{T}{\frac{1}{2}\rho\pi \left(L_b + R_h\right)^2 \left\|\vec{u}^{\infty}\right\|^2}. \tag{5}$$

As the literature [8, 12, 20] reported that the contribution of added mass to the turbine loads in wave and current conditions is limited, it has not been added to the model in the present study. It will be added in a near future as it is known to become important for highly dynamic conditions such as blades pitching motion.

## II – 2 Stokes first order wave-current model

In the presented VP solver, surface gravity waves are modelled through their orbitals motion velocities and the associated gradient. The fluid is subjected to gravity acceleration ($\vec{g} = -g\vec{e}_z$). It is assumed that gravity wave induced flow is irrotational to use the potential theory with a Stokes first order wave-current model. Hence waves only affect Eq. (4). The mean upstream current ($\vec{u}^\infty$) is carried by the $\vec{e}_x$ vector. Waves of given angular velocity ($\omega_w$) propagate along their wave number vector ($\vec{k}_w$) in any of the $(\vec{e}_x, \vec{e}_y, 0)$ plane directions. The angle between the wave number vector ($\vec{k}_w$) and current velocity unitary vector ($\vec{e}_x$) is $\beta$. The reference frame is orthonormal Cartesian and located such that the free surface mean level is at $z = 0$. Within this coordinate system, the position vector variable is $\vec{x} = (x, y, z)$. The free surface crest to trough waves amplitude ($a$) is assumed to be small with respect to the wavelength ($L_w$) and water depth ($h$). Those free-surface-related assumptions are mentioned in the present subsection for the sake of explanation. However, the free surface is currently not modelled in the VP solver in which the fluid domain is unbounded. A check is performed afterwards to ensure that fluid particles do not leave the water column. All the hypothesis are summarized within Figure 1.

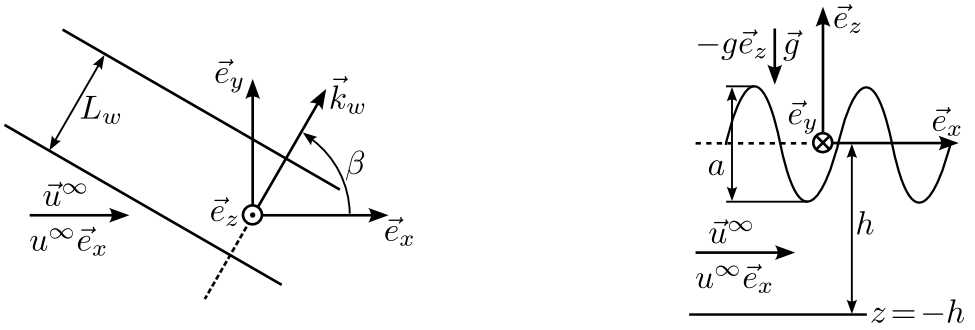


(a) $(\vec{e}_x, \vec{e}_y, 0)$ plane. (b) $(\vec{e}_x, 0, \vec{e}_z)$ plane.

FIGURE 1 – Free surface wave schemes seen from the top ($(\vec{e}_x, \vec{e}_y, 0)$ plane, Subfig. 1a) and from the side ($(\vec{e}_x, 0, \vec{e}_z)$ plane, Subfig. 1b).

Under such assumptions, the three waves orbital velocity components are [18]:

$$u_x^w(\vec{x},t) = \underbrace{a\cos(\beta)\left(\omega_w - u^\infty k_w\cos(\beta)\right)\frac{\cosh(k_w(z+h))}{\sinh(k_w h)}}_{=A(u_x^w)(z)}\sin\left(\xi_w(\vec{x},t)\right), \tag{6}$$

$$u_y^w(\vec{x},t) = a\sin(\beta)\left(\omega_w - u^\infty k_w\cos(\beta)\right)\frac{\cosh(k_w(z+h))}{\sinh(k_w h)}\sin\left(\xi_w(\vec{x},t)\right), \tag{7}$$

$$u_z^w(\vec{x},t) = \underbrace{a\left(\omega_w - u^\infty k_w\cos(\beta)\right)\frac{\sinh(k_w(z+h))}{\sinh(k_w h)}}_{=A(u_z^w)(z)}\cos\left(\xi_w(\vec{x},t)\right), \tag{8}$$

with the phase expression being $\xi_w(\vec{x},t) = \omega_w t - \vec{k_w}\cdot\vec{x}$. The total orbital velocity vector ($\vec{u}^w = (u_x^w, u_y^w, u_z^w)$) is injected in the potential velocity content (Eq. (4)) which then modifies the vortex particles advection (Eq. (1)). The gradient associated to this orbital velocity vector affects the stretching term ($\vec{S}_i(t)V_i$) of the momentum Navier-Stokes equation (Eq. (2)). However, with the presented wave-current model, the diffusion term ($\vec{L}_i(t)V_i$) remains unchanged. To summarize, the presented model needs only a few

inputs to run: water depth ($h$), waves angular frequency ($\omega_w$), crest to trough amplitude ($a$), propagation angle ($\beta$) and wavelength ($L_w$).

## III – Numerical set-up and wave conditions

The numerical set-up of the present study consists in a single tidal turbine model immersed in a mean flow with surface waves. The geometric considerations are based upon the one of the IFREMER wave and current flume tank. The turbine model is the IFREMER-LOMC one of blade length ($L_b = 0.304$ m) and hub radius ($R_h = 0.058$ m). It is discretized into twenty sections ($N_s = 20$) thus providing a spatial resolution of about 1.5 cm. The blades geometry was first presented in [16]. The numerical adaptation for the lifting-line formalism, including the polar curves, is detailed in [7]. The turbine model immersion depth is $z_{rot} = -1$ m which is halfway between the free surface and the flume tank bed with a water depth of two meters ($h = 2$ m). Density ($\rho$) and kinematic viscosity ($\nu$) of the water are set as: $\rho \simeq 10^3$ kg$\cdot$m$^{-3}$ and $\nu \simeq 10^{-6}$ m$^2\cdot$s$^{-1}$. The flow conditions consist in a mean upstream flow velocity $u^\infty = 0.8$ m$\cdot$s$^{-1}$ and a given set of waves properties. This numerical set-up is summarized in the scheme presented in Subfig. 2a. An experimental work carried at IFREMER wave and current flume tank [15] characterizes multiple wave conditions which can correspond to real scale sea states measured at sites of interest for tidal energy [9]. For the present study, two wave cases of same frequency ($f_w$) have been chosen among the ones available in this database so as to validate the wave-current model against experimental data. The wave properties are gathered in Table 1 below. One wave case is following current, meaning the waves propagate along $\vec{e}_x$ direction. It is denoted "Following" or "Following wave" afterwards and corresponds to intermediate depth domain, see $h/L_w$ ratio in Table 1. The other one is opposing current, meaning that waves propagate along $-\vec{e}_x$ direction against the current. It is denoted "Opposing" or "Opposing wave" afterwards and corresponds to deep water conditions.

Table 1 – Wave cases properties.

| Wave case | $a$ [m] | $\beta$ [°] | $f_w$ [Hz] | $L_w$ [m] | $h/L_w$ [-] | $U_r$ [-] |
|---|---|---|---|---|---|---|
| Following | 0.064* | 0 | 0.5 | 8.5 | 0.23 | $7.3 \times 10^{-3}$ |
| Opposing | 0.076* | 180 | 0.5 | 3.3* | 0.61 | $1.3 \times 10^{-3}$ |

The values denoted with an asterisk in Table 1 come from the experimental measurements given in [15]. The wavelength of the following wave case is directly assessed with the wave-current dispersion relation [18] as it brings less uncertainty compared to the experimental value. However, the experimental value of the wavelength is kept for the opposing wave case because, for such current velocity (0.8 m$\cdot$s$^{-1}$), no solution of wave-current dispersion relation is found at this frequency. This case was chosen on purpose to assess whether the described wave-current numerical model (subsection II – 2) would be able to reproduce real-life conditions with sufficient accuracy even though being out of its mathematical domain definition. Furthermore, Ursell number ($U_r$) is computed for each wave case. Very small values as in Table 1 ensure that the wave cases are in the validity domain of the Stokes first order wave-current model.

To validate the wave model orbital $x$ and $z$ velocity components amplitude along the water column are presented respectively in Subfig. 2b and Subfig. 2c. In the Dorothy

solver, both equations (6) and (8) are coded as functions of space and time. This is the reason why some specific points of measurements have been defined in the code to record the time histories of the velocity along the water column. Hence, the amplitude of the sinusoidal signal is obtained through a sine least mean square (LMS) method. This provides the squared measurement points in Subfig. 2b and Subfig. 2c labelled "LMS Num.". To ensure that the wave model was correctly coded, the amplitudes as function of depth ($z$) are also directly evaluated from the expressions of $A(u_x^w)(z)$ an $A(u_z^w)(z)$. Those are the solid lines labelled "Analytical" in Subfig. 2b and Subfig. 2c. Eventually, the dotted lines labelled "Expe." represent the PIV measurements from [15]. First, the equality between the Dorothy LMS numerical results and the analytical amplitudes highlights the correctness of the implementation. Second, a good agreement is found between the numerical points and the experimental data. Hence proving that even for edge-domain cases as the opposing wave one, the model presented in subsection II – 2 is accurate enough to perform tidal turbine under wave studies.

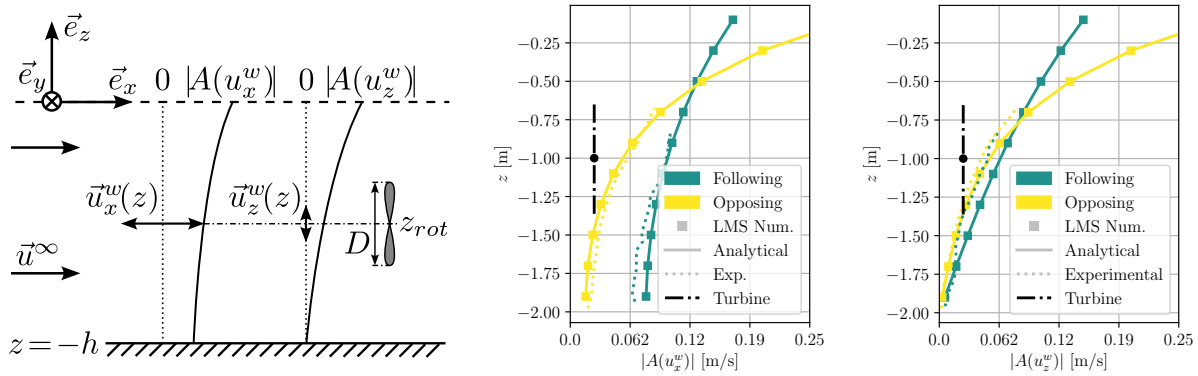


(a) Horizontal axis tidal turbine model set-up conditions.

(b) Wave orbital $x$ velocity component.

(c) Wave orbital $z$ velocity component.

FIGURE 2 – Numerical set-up scheme (Subfig. 2a) and wave orbital velocity profiles from Dorothy time series (LMS Num.) against orbitals amplitude direct evaluation (Analytical) and experimental PIV measurements from [15]. Turbine location is represented.

The tidal turbine model performance are studied across the tip speed ratio range, defined as $TSR = \omega_{rot}(R_h + L_b)/u^\infty$. As the flow velocity is fixed, the turbine angular velocity changes. A constant angular step for turbine rotation of three degrees per time-step is used in the computations. Hence, the time-step (d$t$) varies for each $TSR$ value. Those computations parameters are reported in Table 2. An exception is performed on time-step definition for some wave cases inflow where the dynamic is driven by waves motion. This is highlighted in parenthesis in Table 2. The computations run on 192 to 1152 CPUs on AMD EPYC 9654 Genoa nodes with a wall-clock time ranging from one hour (low $TSR$) to twenty six hours (high $TSR$ with wave and long wakes simulation).

TABLE 2 – Studied $TSR$ and time discretization.

| $TSR$ [-] | 1 | 2 | 3 | 3.25 | 3.5 | 3.75 | 4 | 5 | 6 | 7 |
|---|---|---|---|---|---|---|---|---|---|---|
| $\omega_{rot}$ [rad·s$^{-1}$] | 2.21 | 4.42 | 6.63 | 7.18 | 7.74 | 8.29 | 8.84 | 11.1 | 13.3 | 15.5 |
| d$t$ [$\times 10^{-2}$s] | 2.4 | 1.2 (0.59) | 0.79 | 0.73 | 0.68 | 0.63 | 0.59 | 0.47 | 0.39 (0.34) | 0.34 |

# IV – Wave effects on tidal turbine performance and wake

## IV – 1 Performance and loads results

First, the time series of the turbine performance at $TSR = 4$ are presented in Fig. 3. The quasi steady results (dark blue) are shown as baseline reference in front of the two wave cases: following (green) and opposing (yellow). The computations start with a transient state until time $t \simeq 4$ s. It is easily discernable on the quasi steady results where both power and thrust coefficients (resp. $C_P$ and $C_T$, Eq. (5)) goes through a maximum before slowly converging towards the steady values. The transient domain corresponds to time needed for the wake to grow farther than four turbine diameters ($4D$). Indeed when the wake reaches $4D$, less than 1 % of error is done on the axial velocity evaluation (Eq. (3)) at the turbine position [3]. Concerning the two wave cases, significant performance fluctuations occur. The wave-induced fluctuations are of opposite phase due to the influence of opposite direction of propagation on Eq. (6) to Eq. (8).

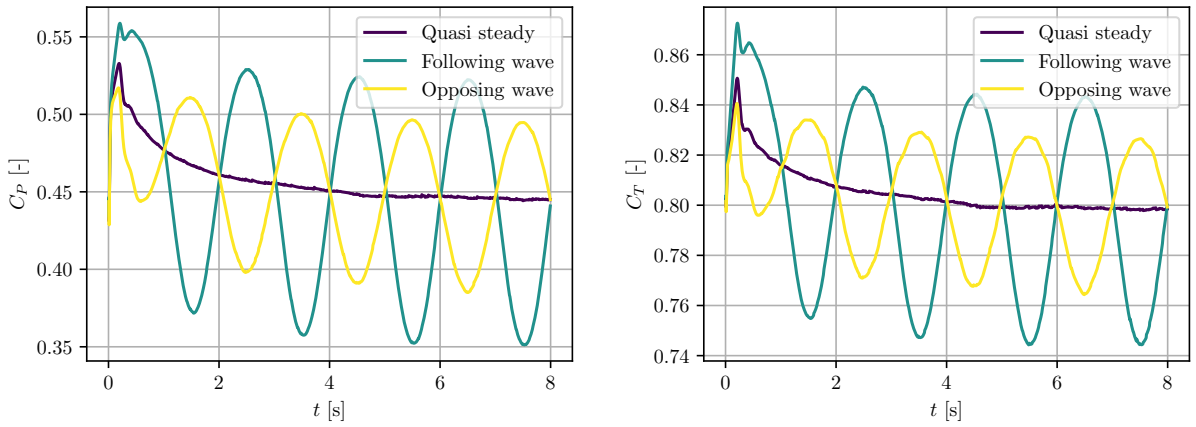


(a) Power coefficient ($C_P$). (b) Thrust coefficient ($C_T$).

FIGURE 3 – Time histories of the turbine model performance at $TSR = 4$. The two wave cases are reported against the quasi steady results as reference.

Performance results against $TSR$ are presented in Fig. 4. The values are averaged over the last two seconds of each eight-second computation. This ensures to have converged loads and also a complete wave period ($T_w = 2$ s) for the wave cases to correctly assess average and standard deviation. It is noticed that no significant change in average values is introduced by following or opposing wave cases with respect to the quasi steady reference. This observation matches the results available in the literature both from experimental [14, 4, 11] and numerical sides [1, 8, 12, 20]. The standard deviation is at such a low level on the quasi steady curve that it is not discernable in Fig. 4. This relates to the flow steadiness: no upstream turbulence and no turbine angular velocity ($\omega_{rot}$) variations. Nevertheless, significant standard deviations are observed for the wave cases. Wave-induced standard deviations are increasing with $TSR$ for both power and thrust coefficients. This behaviour and the order of magnitudes presented are consistent with [11]. Eventually, Fig. 4 highlights that the turbine suffers higher performance fluctuations in the following wave case than in the opposing one. This is due to the wave orbitals velocity amplitudes which are significantly greater along the turbine area for the following wave case as shown in Fig. 2b and Fig. 2c.

The radial distributions of angles of attack ($\alpha$), local tangential ($\mathrm{d}F_\theta$) and axial ($\mathrm{d}F_x$)

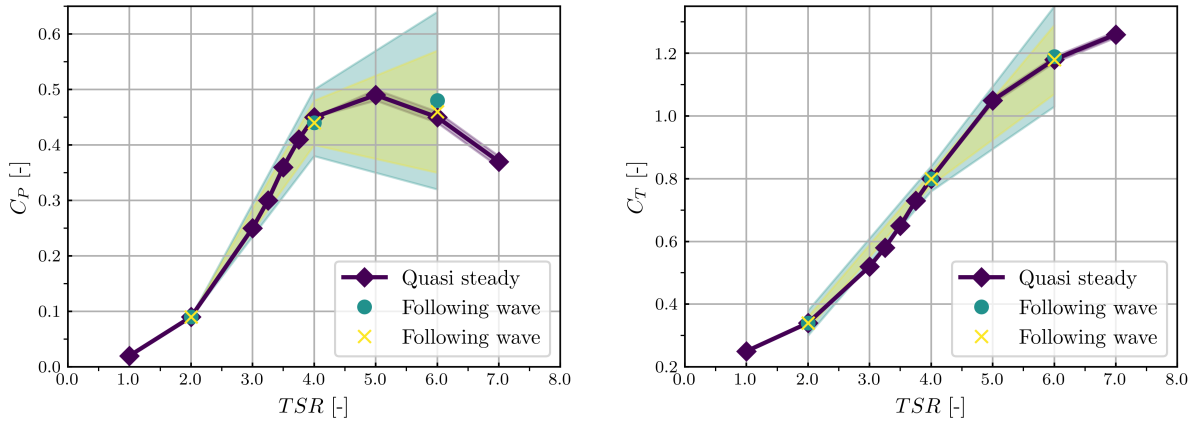


(a) Power coefficient ($C_P$). (b) Thrust coefficient ($C_T$).

FIGURE 4 – Turbine performance as a function of $TSR$. The two wave cases are reported against the quasi steady computations as reference. Each point represents the average and the standard deviation is the lightly coloured area.

forces of one blade of the turbine at $TSR = 4$ are respectively presented in Subfig. 5a, Subfig. 5b and Subfig. 5c. The average (solid line) with the associated standard deviation (lightly coloured area) are plotted in dark blue for the quasi steady case, green for the following wave case and yellow for the opposing one. Note that $R = R_h + L_b$. The local fluctuations of angles of attack decrease when approaching blade tip. Near blade tip the rotation tangential velocity contribution to the local velocity is increasingly important. This makes the wave-induced velocity fluctuations in the axial direction ($u_x^w$) relatively lower, thus decreasing the amplitude of angle of attack variations. In addition, Subfig. 5b and Subfig. 5c show that, relatively to the mean value, higher fluctuations are noticed for the tangential loads (generating power) than for the axial loads (generating thrust). Eventually, maximum loads fluctuations is located around 70 % of the rotor radius ($R = R_h + L_b$).

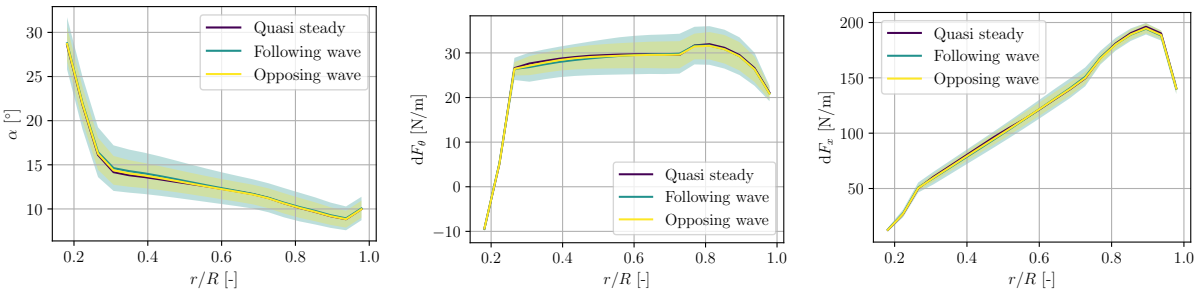


(a) Angle of attack. (b) Tangential force. (c) Axial force.

FIGURE 5 – Radial distributions of angles of attack ($\alpha$), local tangential ($dF_\theta$) and axial ($dF_x$) forces of the turbine model at $TSR = 4$ with standard deviation at each location. The two wave cases are reported against the quasi steady computation as reference.

## IV – 2 Wake analysis at $TSR = 4$

The wake study consists in instantaneous axial velocity maps in $(\vec{e}_x, 0, \vec{e}_z)$ plane at four phase-locked times with respect to the wave motion for both following (Fig. 6) and

opposing (Fig. 7) wave cases. Four specific times are defined ($t_0, t_{90}, t_{180}, t_{270}$). The time $t_0$ is a multiple of the wave period ($t_0 \equiv 0 \pmod{T_w}$). Then, each time equals to the previous one with an increment of a quarter of the wave period. Those four specific times ensure that the wave phase ($\xi_w$) at the turbine rotation centre ($x_{rot} = y_{rot} = 0$ m) is respectively 0° (Subfig. 6a and Subfig. 7a), 90° (Subfig. 6b and Subfig. 7b), 180° (Subfig. 6c and Subfig. 7c) and 270° (Subfig. 6d and Subfig. 7d). An analytic free surface ($\eta = a\sin(\xi_w(\vec{x}, t))$) is reconstructed above each velocity phase-locked map to better relate wave motion with the flow. The free surface is represented in this manner as no free surface is modelled in the presented formalism (section II). This representation reproduces experimental PIV visualizations taken in the near wake behind a tidal turbine model and available in [13].

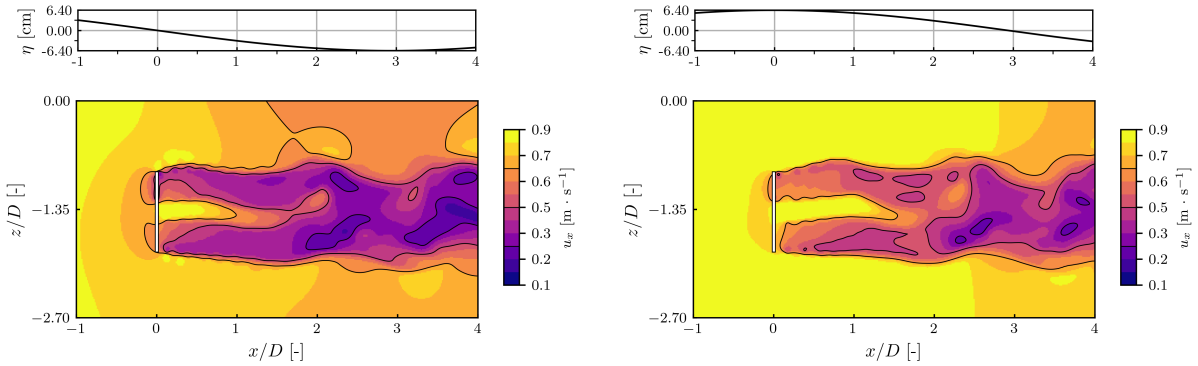


(a) 0° phase.

(b) 90° phase.

(c) 180° phase.

(d) 270° phase.

FIGURE 6 – Following waves phase-locked instantaneous axial velocity maps up to $4D$ past the tidal turbine. An analytical free surface is reconstructed above each map for the sake of clarity.

In the following wave case (Fig. 6), the wave-induced velocity change compared to the mean upstream flow velocity consists in overspeed areas under wave crest and underspeed areas under wave trough. This is consistent with the reported motion in [4]. In the opposing wave case (propagation direction opposite to the current, Fig. 7), it is worth noting that the wave crests are associated with underspeed areas and wave trough are associated with overspeed regions. Furthermore, for both following and opposing wave cases, waves generate a periodic motion, or meandering, of the tidal turbine wake. The tidal turbine wake is alternatively uplifted in front of wave crest in the wave propagation direction and downlifted in front of wave trough. This wave-induced tidal turbine wake periodic motion

is easily noticeable for the following wave case. A similar behaviour in a tidal turbine wake has been experimentally reported in [13]. Finally, to the author's opinion, such vertical motion of tidal turbine wake may increase vertical transport of energy, thus helping wake recovery and re-energizing as shown in a comprehensive numerical study [17].

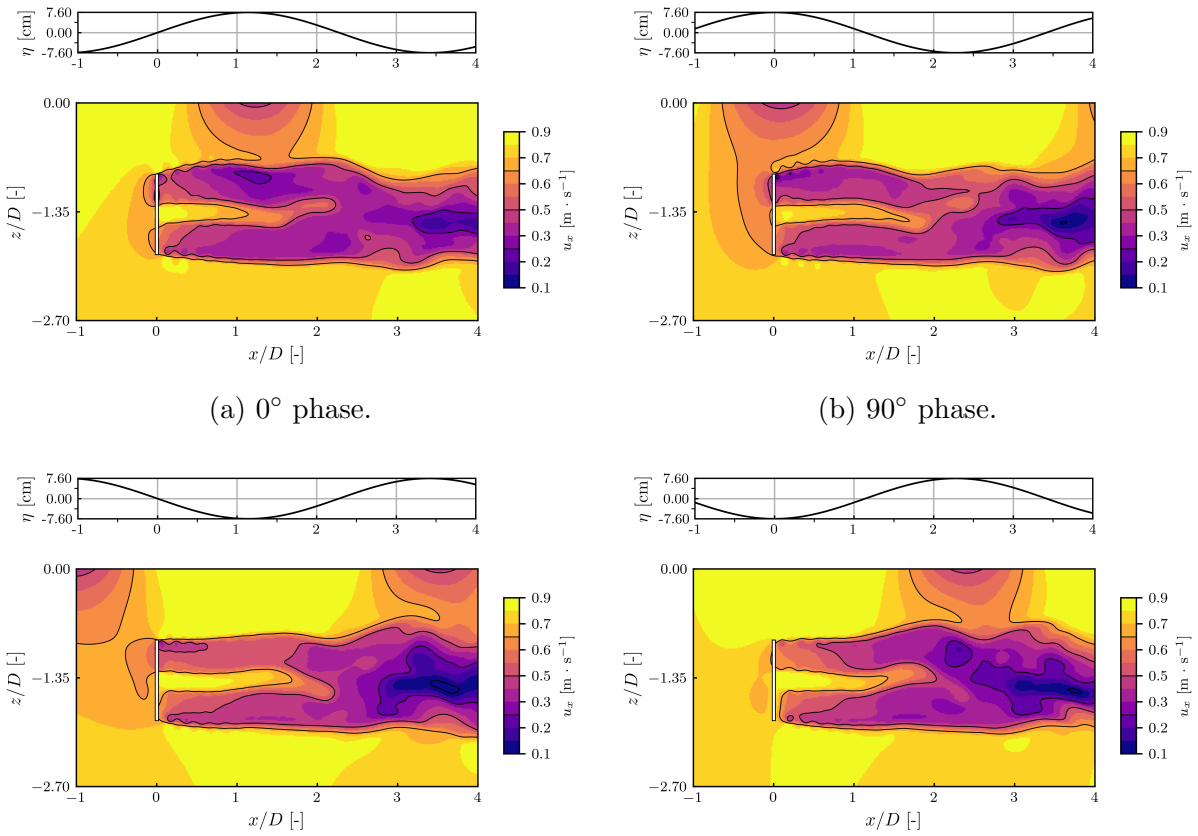


(a) 0° phase.

(b) 90° phase.

(c) 180° phase.

(d) 270° phase.

FIGURE 7 – Opposing waves phase-locked instantaneous axial velocity maps up to $4D$ past the tidal turbine. An analytical free surface is reconstructed above each map for the sake of clarity.

## V – Conclusion

To summarize, the Stokes first order wave-current potential model has been validated against experimental orbitals velocity data. The results show that this wave model works properly even for the opposing wave case with so closed edge-domain entries. Waves influence on tidal turbine performance is accurately modelled with the presented wave model added to the vortex particle (VP) solver Dorothy with a lifting-line (LL) turbine blades representation. Turbine averaged performance remains unaffected by waves but with a significant increase of standard deviations correlated with the tip speed ratio. The asymmetric wave-induced loads fluctuations between turbine torque and thrust is also noticed. Moreover, the presented method allows to investigate wave-induced periodic motions in the tidal turbine wake meandering at a limited computational cost. It is shown that tidal turbine wake is alternatively uplifted in front of wave crest and downlifted in front of wave trough, both in the wave propagation direction. Those two last elements highlight the relevance of this wave model choice to carry such investigations. Furthermore, it high-

lights the importance of taking gravity waves into account when assessing tidal turbine blades fatigue or wake interactions in a farm array. All this elements give confidence in the presented approach. It opens a path towards numerical parametric studies using this methodology. However a lot remains to be done with the addition of an added mass model and a dynamic stall model to possibly blend the waves with highly dynamic conditions as upstream turbulence or turbines wake interaction.

## Acknowledgement

The authors acknowledge the support of IFREMER and the Normandy Region for the funding of the present PhD work. The numerical results are obtained using computing resources of CRIANN (Normandy, France). The authors acknowledge Gabriel MERCEUR for having conducted the preliminary studies on the topic during his IFREMER internship.

## Références

[1] N. Barltrop, K. S. Varyani, A. Grant, D. Clelland, and X. P. Pham. Investigation into wave-current interactions in marine current turbines. *Proceedings of the Institution of Mechanical Engineers, Part A: Journal of Power and Energy*, 221(2):233–242, Mar. 2007.

[2] J.-P. Choquin and G.-H. Cottet. Sur l'analyse d'une classe de méthodes de vortex tridimensionnelles. *Comptes Rendus Hebdomadaires des Séances de l'Académie des Sciences*, 306(17):739–742, May 1988.

[3] R. Corniglion. *Aero-Elastic Modeling of Floating Wind Turbines with Vortex Methods.* These de doctorat, Marne-la-vallée, ENPC, June 2022.

[4] T. De Jesus Henriques, S. Tedds, A. Botsari, G. Najafian, T. Hedges, C. Sutcliffe, I. Owen, and R. Poole. The effects of wave–current interaction on the performance of a model horizontal axis tidal turbine. *International Journal of Marine Energy*, 8:17–35, Dec. 2014.

[5] P. Degond and S. Mas-Gallic. The weighted particle method for convection-diffusion equations - Part II : The anisotropic case. *Mathematics of Computation*, 53:509–526, 1989.

[6] S. Draycott, J. Steynor, A. Nambiar, B. Sellar, and V. Venugopal. Rotational sampling of waves by tidal turbine blades. *Renewable Energy*, 162:2197–2209, Dec. 2020.

[7] M.-A. Dufour, G. Pinon, E. Rivoalen, F. Blondel, and G. Germain. Development and validation of a lifting-line code associated with the vortex particle method software Dorothy. *Wind Energy*, 27(7):633–666, July 2024.

[8] C. Faudot and O. G. Dahlhaug. Prediction of wave loads on tidal turbine blades. *Energy Procedia*, 20:116–133, 2012.

[9] J.-F. Filipot, M. Prevosto, C. Maisondieu, M. Le Boulluec, and J. Thomson. Wave and turbulence measurements at a tidal energy site. In *2015 IEEE/OES Eleventh Current, Waves and Turbulence Measurement (CWTM)*, pages 1–9, St. Petersburg, FL, Mar. 2015. IEEE.

[10] B. Gaurier, C. Carlier, G. Germain, G. Pinon, and E. Rivoalen. Three tidal turbines in interaction: An experimental study of turbulence intensity effects on wakes and turbine performance. *Renewable Energy*, 148:1150–1164, Apr. 2020.

[11] B. Gaurier, S. Ordonez-Sanchez, J.-V. Facq, G. Germain, C. Johnstone, R. Martinez, F. Salvatore, I. Santic, T. Davey, C. Old, and B. Sellar. MaRINET2 Tidal Energy Round Robin Tests—Performance Comparison of a Horizontal Axis Turbine Subjected to Combined Wave and Current Conditions. *Journal of Marine Science and Engineering*, 8(6):463, June 2020.

[12] X. Guo, J. Yang, Z. Gao, T. Moan, and H. Lu. The surface wave effects on the performance and the loading of a tidal turbine. *Ocean Engineering*, 156:120–134, May 2018.

[13] E. E. Lust, K. A. Flack, and L. Luznik. Survey of the near wake of an axial-flow hydrokinetic turbine in the presence of waves. *Renewable Energy*, 146:2199–2209, Feb. 2020.

[14] L. Luznik, K. A. Flack, E. E. Lust, and K. Taylor. The effect of surface waves on the performance characteristics of a model tidal turbine. *Renewable Energy*, 58:108–114, Oct. 2013.

[15] M. Magnier. *Étude expérimentale de l'effet des courants de marée et de la houle sur la dynamique tourbillonnaire d'une variation bathymétrique et sur le comportement d'une hydrolienne*. PhD thesis, Université de Lille, 2023.

[16] P. Mycek. *Étude Numérique et Expérimentale Du Comportement d'hydroliennes*. PhD thesis, Université du Havre, 2013.

[17] P. Ouro, H. Mullings, A. Christou, S. Draycott, and T. Stallard. Wake characteristics behind a tidal turbine with surface waves in turbulent flow analyzed with large-eddy simulation. *Physical Review Fluids*, 9(3):034608, Mar. 2024.

[18] O. M. Phillips. *The Dynamics of the Upper Ocean*. Cambridge Monographs on Mechanics and Applied Mathematics. Cambridge University Press, Cambridge, 2. ed edition, 1977.

[19] J. Saverin, D. Marten, G. Pechlivanoglou, and C. O. Paschereit. Advanced Medium-Order Modelling of a Wind Turbine Wake with a Vortex Particle Method Integrated within a Multilevel Code. *Journal of Physics: Conference Series*, 1037:062029, June 2018.

[20] G. T. Scarlett, B. Sellar, T. Van Den Bremer, and I. M. Viola. Unsteady hydrodynamics of a full-scale tidal turbine operating in large wave conditions. *Renewable Energy*, 143:199–213, Dec. 2019.

[21] P. Singh and P. Friedmann. A Computational Fluid Dynamics Based Viscous Vortex Particle Method for Coaxial Rotor Interaction Calculations. In *Proceedings of the Vertical Flight Society 73rd Annual Forum*, pages 1–8, Fort Worth, Texas, May 2017. The Vertical Flight Society.

[22] J. Valentin and L. Bernardos. Validation of a new solver based on the vortex particle method for wings, propellers and rotors. In *49th European Rotorcraft Forum 2023 - Proceedings*, volume S.1-26, Bückeburg, Germany, Sept. 2023. DGLR-Bericht, Deutsche Gesellschaft für Luft- und Raumfahrt - Lilienthal-Oberth e.V., Bonn.

[23] G. S. Winckelmans and A. Leonard. Contributions to vortex particle methods for the computation of three-dimensional incompressible unsteady flows. *Journal of Computational Physics*, 109(2):247–273, 1993.